Compositional Neural Scene Representations for Shading Inference

JONATHAN GRANSKOG, ETH Zurich & NVIDIA
FABRICE ROUSSELLE, NVIDIA
MARIOS PAPAS, DisneyResearch|Studios
JAN NOVÁK, NVIDIA

We present a technique for adaptively partitioning neural scene representations. Our method disentangles lighting, material, and geometric information yielding a scene representation that preserves the orthogonality of these components, improves interpretability of the model, and allows compositing new scenes by mixing components of existing ones. The proposed adaptive partitioning respects the uneven entropy of individual components and permits compressing the scene representation to lower its memory footprint and potentially reduce the evaluation cost of the model. Furthermore, the partitioned representation enables an in-depth analysis of existing image generators. We compare the flow of information through individual partitions, and by contrasting it to the impact of additional inputs (G-buffer), we are able to identify the roots of undesired visual artifacts, and propose one possible solution to remedy the poor performance. We also demonstrate the benefits of complementing traditional forward renderers by neural representations and synthesis, e.g. to infer expensive shading effects, and show how these could improve production rendering in the future if developed further.

CCS Concepts: • **Computing methodologies → Rendering**; **Neural networks**.

Additional Key Words and Phrases: rendering, neural networks, neural scene representations, disentanglement, attribution

ACM Reference Format:
Jonathan Granskog, Fabrice Rousselle, Marios Papas, and Jan Novák. 2020. Compositional Neural Scene Representations for Shading Inference. *ACM Trans. Graph.* 39, 4, Article 135 (July 2020), 13 pages. https://doi.org/10.1145/3386569.3392475

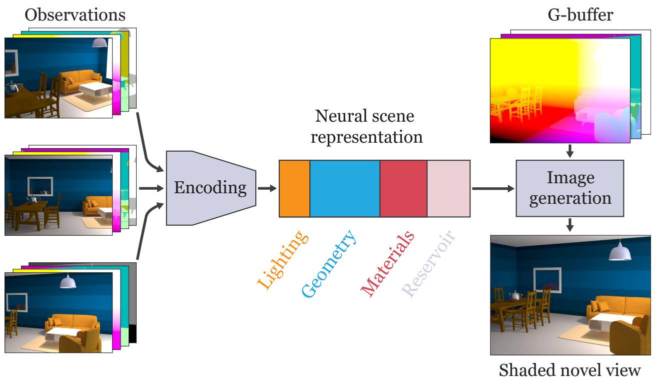

Fig. 1. We present an approach for extracting adaptively partitioned, compressible neural scene representations of 3D scenes that disentangle lighting, material, and geometry information. The compositionality of the representation aids interpretability and analysis of the inner workings of the model, which are key for remedying visual artifacts and combining neural approaches with traditional forward renderers.

1 INTRODUCTION

Data-driven realistic image synthesis has recently achieved a number of notable breakthroughs, such as rendering realistic human faces [Karras et al. 2018], or high-quality relighting of photographs [Philip et al. 2019]. Remarkable achievements have been demonstrated also in data-driven simulation of light transport, where neural networks predict various radiative quantities [Hermosilla et al. 2019; Kallweit et al. 2017; Nalbach et al. 2017; Ren et al. 2013] or improve their unbiased estimation [Müller et al. 2019; Zheng and Zwicker 2019]. Common to all these is the utilization of neural networks to perform the task in its entirety, all at once. The black-box nature, however, hinders interpretability, generalization, and makes further development less intuitive.

An alternative approach to performing the synthesis at once is to introduce an intermediate neural scene representation [Eslami et al. 2018; Kulkarni et al. 2015; Sitzmann et al. 2019], by breaking the rendering task into: (i) extracting a learned scene representation, and (ii) using it to render an image. The intermediate (latent) scene representation allows enforcing certain behaviors upon the model, e.g. ensuring consistency of images rendered from different views of the scene. It also presents an opportunity for increasing robustness, improving generalization, and accelerating training by injecting physically-based constraints to regularize the model. While the scene complexity and rendering quality of these approaches may appear limited at present, it is foreseeable that these will improve in the future, especially if the neural renderer merely *augments* classical rendering pipelines. The key advantage of the neural approach is the end-to-end training, which allows the neural representation to carry information that is complementary to classical inputs and tailored to the task at hand. We carry out our investigations in one such scenario, where a classical rasterizer determines directly visible objects and the neural renderer infers their appearance.

We present two distinct contributions in this article. First, we extend the works of Eslami et al. [2018] and Sitzmann et al. [2019] with mechanisms to disentangle material, lighting, and geometric content of the scene. We do not prescribe a specific encoding between images and the latent scene representation (this shall be extracted from data), but we introduce additional constraints to *adaptively partition* the latent scene representation. The adaptive partitioning ameliorates interpretability of the representation, permits tracing

Authors' addresses: Jonathan Granskog, ETH Zurich & NVIDIA, jgranskog@nvidia.com; Fabrice Rousselle, NVIDIA, frousselle@nvidia.com; Marios Papas, DisneyResearch|Studios, marios.papas@disneyresearch.com; Jan Novák, NVIDIA, jnovak@nvidia.com.

0730-0301/2020/7-ART135
https://doi.org/10.1145/3386569.3392475

the roots of poor rendering quality, and allows compressing the neural scene representation.

Our second contribution, enabled by the adaptive partitioning, is an analysis of generated images with respect to the extracted scene representation and the encoded observations. The analysis yields valuable insights into the inner mechanisms of the neural model and guides the design of techniques for remedying objectionable artifacts and poor performance. Specifically, attributing pixel colors in problematic regions to individual partitions revealed lack of geometric information in the representation; an issue that we address by adding an auxiliary image generator to steer the model towards capturing more geometry.

While the primary focus in this article is on disentanglement and compositionality, we also tease with an example of how neural scene representations could augment classical game and film renderers in the future. We use a ray tracer to render an image with direct illumination, and combine it with an indirect-illumination image synthesized by the neural image generator. Employing neural scene representations in such scenarios enjoys a different set of constraints and conveniences than other (e.g. computer vision) problems. We exploit the main convenience—the existence of a 3D scene model—and provide the neural generator with geometry information (G-buffer) of novel views. We draw inspiration and architectures from works where a 3D model is not available; the focus is on extracting it [Eslami et al. 2018; Sitzmann et al. 2019], but we leverage these architectures to complement the strengths of classical renderers, rather than replacing them. Finally, we demonstrate the benefits of compositional neural scene representations on the application of relighting: we create novel scene configurations by exchanging lighting partitions of different scenes.

Scope. Our method partitions the neural representation via explicit constraints enforced during training. The underlying neural model is non-probabilistic and relies on inputs from classical renderers. Nevertheless, the proposed mechanism for encoding adaptive, compressible neural representations is universal and applicable to other neural architectures and approaches.

2 RELATED WORK

Next, we review recent methods utilizing neural networks for rendering, discuss techniques for representation learning, disentanglement, and attribution, and point out hybrid renderers that bear similarities to our approach. We refer the reader to a recent survey by Tewari et al. [2020] for a more complete overview.

Neural scene representations. A recurring approach to render a scene using neural networks is to start from a voxel grid representation, along with a camera pose and light position. This has been applied to simple shading models [Nguyen-Phuoc et al. 2018] or to a single object with global illumination [Rematas and Ferrari 2019]. Our method can also render these effects, but is not restricted to a single object, and can scale to more complex scenes as it does not incur the memory overhead of a voxel grid. Lombardi et al. [2019] reduce the memory requirements and artifacts of voxel grids, while Sitzmann et al. [2019] replace it altogether with a learned 3D scene representation obtained using a differentiable ray-marcher.

Tatarchenko et al. [2016] compress a single image into a representation for novel view synthesis. Rendering of novel views is also achieved by Thies et al. [2019] who learn neural textures of objects. However, all lighting and shading is "baked" and cannot be edited easily. Our method is designed to avoid such baking. We build upon generative query networks (GQNs) [Eslami et al. 2018], which are composed of two core components: an encoder that extracts a scene representation from multiple observations, and a generator that synthesizes the novel view. The lengthy optimization procedure of GQNs (weeks of training) led to the development of more efficient losses [Nguyen-Ha et al. 2019] and exploitation of geometric information [Tobin et al. 2019]. We take a different approach: we accelerate image generation by leveraging geometric features of the novel view (G-buffer) and using the pixel generator [Sitzmann et al. 2019] architecture instead of the original probabilistic approach utilizing LSTM cores [Eslami et al. 2018]. This significantly accelerates training (days instead of weeks) and improves accuracy.

Disentanglement and user control. Disentanglement has been presented as a key attribute of robust representations [Bengio et al. 2013] and interpretability [Chen et al. 2016], but also as crucial to controllable generation [Nie et al. 2020]. Multiple approaches have been explored to introduce user control, such as latent-space transformations [Nguyen-Phuoc et al. 2019; Olszewski et al. 2019], or disentanglement of the latent variables using unsupervised [Chen et al. 2016; Higgins et al. 2017] or (semi-)supervised methods [Kulkarni et al. 2015; Nie et al. 2020]. Our work builds upon the technique proposed by Kulkarni et al. [2015]: they modify a single aspect of the scene per training batch and average the activations and adjust gradients for partitions encoding other (static) aspects. We employ this technique to partition lighting, material, and geometry in the representation, and extend it to obtain adaptively partitioned, compressed scene representations.

Interpretability and Attribution. An underlying goal of our work is to gain insights into data-driven image synthesis by attributing the outputs to individual components of the model. Du et al. [2019] classify interpretability as either global or local. Global interpretation, which relates a model behavior to the network parameters and structure, is facilitated by our proposed adaptive partition scheme. Local interpretability, which relates a model output to its inputs, can be achieved through perturbation-based [Wagner et al. 2019; Zeiler and Fergus 2014] and gradient-based [Ancona et al. 2018; Shrikumar et al. 2017] methods; we use the latter type. While these are commonly used in the context of classification, we perform attribution on a pixel basis, that is, we attribute each pixel value to the extracted scene representation, which in turn can be related to the input observations to get a complete view of data flow.

Hybrid Renderers. Augmenting traditional renderers using data-driven techniques has a long and successful history. Early successes in data-driven lighting [Debevec 1998] and material modeling [Debevec et al. 2000; Matusik 2003] have had a profound impact on rendering pipelines, both for real-time and offline applications. Recent work has turned to deep learning techniques, for instance to model subsurface scattering [Vicini et al. 2019], approximate multiple scattering in clouds [Kallweit et al. 2017], or approximate light

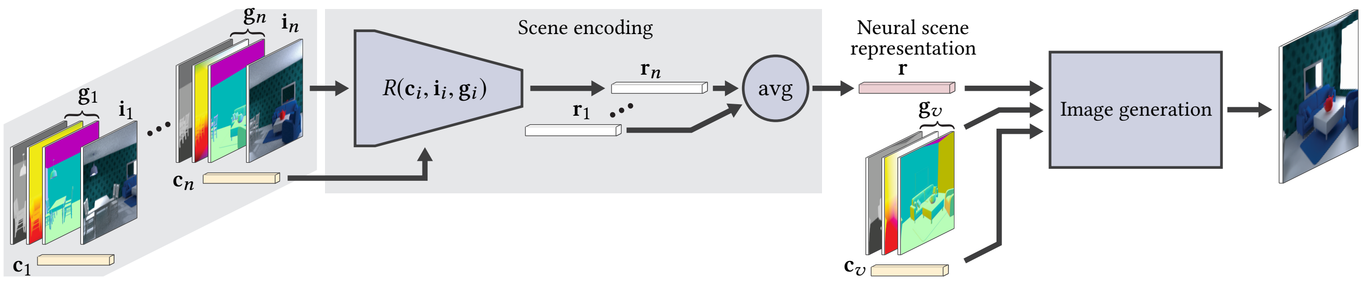

Fig. 2. In order to generate an image, we utilize a view-independent neural scene representation $\mathbf{r}$ and a G-buffer rendered using a classical renderer from a novel view v. The scene representation is extracted from n (high-quality) observations of the scene. Each i-th observation, which consists of a color image $\mathbf{i}_i$, G-buffer $\mathbf{g}_i$, and camera parameters $\mathbf{c}_i$, is processed using a neural encoder to produce a vector $\mathbf{r}_i$. These vectors are averaged across all observations to obtain the neural scene representation $\mathbf{r}$ (pink box). For a novel view v, the representation $\mathbf{r}$, camera parameters $\mathbf{c}_v$, and G-buffer $\mathbf{g}_v$ are fed into an image-generating neural network to obtain an image of the scene from v. This model is largely similar to the one proposed by Eslami et al. [2018]—the main difference is the use of G-buffers. The focus of this paper is on adaptively partitioning the neural scene representation $\mathbf{r}$.

transport in screen space [Nalbach et al. 2017]. Hybrid renderers have also gained traction in computer vision applications, such as video retargeting [Kim et al. 2018], due to their increased realism. Similarly to these approaches, we propose to integrate data-driven image synthesis in the rendering pipeline, but we do so in a more general setting allowing the model to synthesize arbitrary (residual) components of light transport, which complement existing rendering techniques. We show examples where the image generator translates a G-buffer into a shaded image, or a G-buffer with direct illumination into an indirectly lit image only. Our model bears similarities with Deep Shading [Nalbach et al. 2017]; the main difference is the utilization of the neural scene representation (and the encoder) that provides complementary information to the G-buffer.

3 BACKGROUND AND MODEL OVERVIEW

Our goal is to leverage neural scene representations to improve traditional forward-rendering tasks, in which a virtual 3D scene is rendered into a 2D image. We draw inspiration from prior works, where one neural network—scene encoder—builds a scene representation that is then passed to another network—image generator—that synthesizes a novel image of the scene [Eslami et al. 2018; Kulkarni et al. 2015; Sitzmann et al. 2019].

The individual components of our rendering system (see Figure 2) are based on previously published techniques; we do not claim novelty in their design. Our original contributions, described in Section 4 and Section 5, pertain to the combination of these components, as well as the optimization and analysis of the resulting model.

The rest of this section discusses individual components of the model, the inputs, datasets, and loss functions used in our tests.

3.1 Scene encoder

The task of the scene encoder is to extract relevant information from n scene observations $\{(\mathbf{c}_i, \mathbf{i}_i, \mathbf{g}_i)\}_{i=1..n}$ and compress it into a *neural scene representation* $\mathbf{r}$. In our case, observation i consists of a view matrix identifying the camera view $\mathbf{c}_i$, a color image $\mathbf{i}_i$ that contains all light transport we wish to reproduce later, and a G-buffer $\mathbf{g}_i$ that contains geometry features of visible surfaces obtained as a byproduct of rendering the color image.

The main component of the encoder is a convolutional neural network R, which extracts a partial, high-dimensional scene representation $\mathbf{r}_i$ for each observation i: $\mathbf{r}_i = R(\mathbf{c}_i, \mathbf{i}_i, \mathbf{g}_i)$. We use the *pool* architecture [Eslami et al. 2018] for the encoding network R. The network takes a tensor of concatenated image buffers $(\mathbf{i}_i, \mathbf{g}_i)$ and processes them with strided convolutions. The viewpoint parameters $\mathbf{c}_i$ are shaped into a tensor and concatenated to the output tensor of one of the convolutional layers in the middle of the network. The last component of the network is a pooling layer that outputs a $1 \times 1 \times k$ vector $\mathbf{r}_i$ where k is the number of desired values in representations; see [Eslami et al. 2018] for details.

All partial representations are combined to obtain a (more) complete representation of the scene using an order-independent aggregator; we use componentwise averaging: $\mathbf{r} = \text{avg}\left(\{\mathbf{r}_i\}_{k=1..n}\right)$. Alternative aggregators such as summation, attention networks, and max pooling have been explored by Eslami et al. [2018], Rosenbaum et al. [2018], and Deschaintre et al. [2019], respectively.

3.2 Image Generator

The purpose of the image generator is to synthesize an image from a novel, unobserved view v of the scene. The generator receives: (i) parameters of the camera $\mathbf{c}_v$, (ii) a G-buffer $\mathbf{g}_v$ rendered using a traditional renderer from the novel view v, and (iii) a view-independent scene representation $\mathbf{r}$ extracted by the encoder.

Numerous architectures have been proposed for neural image synthesis. In what follows, we utilize two image-to-image translation models: the convolutional U-net architecture [Ronneberger et al. 2015] and the pixel generator [Sitzmann et al. 2019].

The main strength of the convolutional U-net is the large receptive field, i.e. the ability to source information from distant pixels in the G-buffer. In contrast, the pixel generator—being a simple multilayer perceptron—processes each pixel independently and cannot rely on pixel neighborhoods; this has been leveraged as a strength to ensure multi-view consistency [Sitzmann et al. 2019].

Please see the supplementary material for illustrations of the architectures, implementation details, and an expanded analysis of the strengths and weaknesses including also the GQN generator proposed by Eslami et al. [2018].

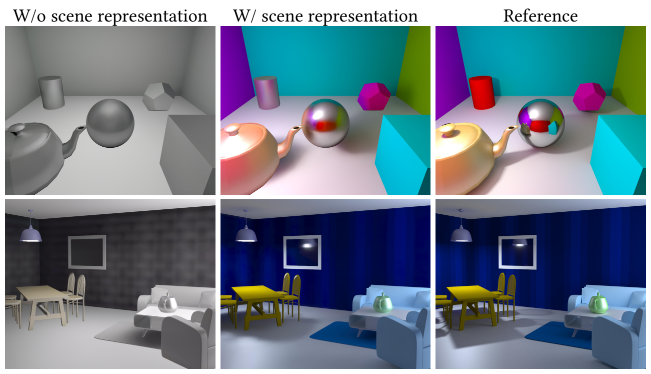

Fig. 3. In most of our experiments, the neural scene representation provides all material and lighting information, and information about geometry outside the camera frustum. Without it (left) the image generator can still synthesize images using the information in the G-buffer, but it learns to produce average appearances and lighting in the training set.

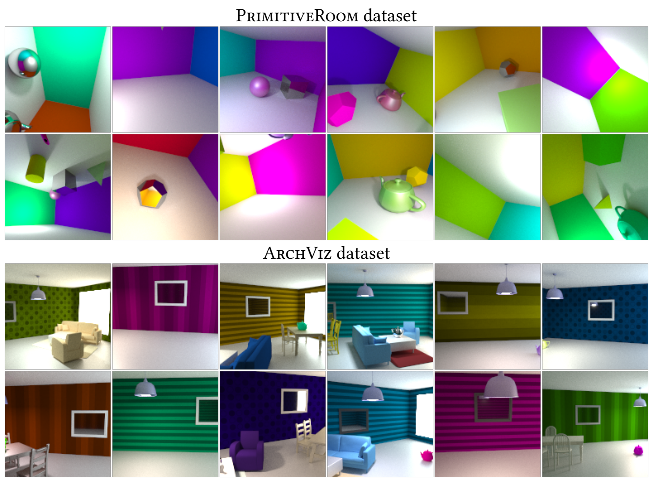

Fig. 4. Random scenes from the PrimitiveRoom and the ArchViz datasets.

3.3 G-buffer Content

The encoder and the generator utilize G-buffers rendered from the observed locations and from the novel view, respectively. This has the benefit of accelerating the optimization, improving the image quality, and allowing smaller, faster image generators to perform well. In this paper, the decision of what surface features to include in the G-buffer is driven by the ease of analysis and interpretability of the learned scene representation. We chose to include only *geometry* information in the G-buffer, namely world-space *positions*, *normals*, and *object identifiers*. Information about materials, lighting, and offscreen or occluded geometry is delivered to the generator only through the neural scene representation. Figure 3 demonstrates the impact of the scene representation on generated images.

The distinct separation of scene properties allows analyzing the flow of information inside the model. A more practical scenario, where the G-buffer contains also material and lighting information, is discussed in Section 6.1.

3.4 Datasets and Optimization

We use two datasets in our experiments. Each dataset consists of 144k procedurally generated instances; a detailed generation recipe is provided in the supplementary material. The color images (see Figure 4 for examples) were rendered using path tracing and feature multi-bounce effects, such as color bleeding and mirror reflections.

The visually simple PrimitiveRoom dataset contains rectangular rooms with a small number of geometric primitives. The primitives vary in shape, position, and rotation and feature a random instance of either a Lambertian diffuse material, a glossy material, or an ideal mirror. The scene is illuminated by a single spherical emitter.

The ArchViz dataset consists of variations of a living room with a dining area. While still rather simple, the geometry, materials, and lighting are biased towards an apartment design. The variations are created by randomizing the luminaire and furniture placement, and by varying the (textured) albedo and roughness of materials.

Optimization. We train the models end-to-end using the Adam optimizer [Kingma and Ba 2015] with a learning rate of 10^{-4} and minibatches consisting of 16 scenes. For each scene, we construct the neural scene representation by encoding three random observations with 64×64 resolution. The resolution of the G-buffer $\mathbf{g}_v$ fed into the image generator is also 64×64 during training, but it is increased at test time in most of our figures. We use a loss comprising a pixelwise L1 error term and a structural dissimilarity (DSSIM) term, which we empirically found to work well when scaled to have approximately equal magnitude. We optimize using one million batches, which amounts to 111 training epochs and requires about 8.5 days of training on a single NVIDIA Tesla V100 GPU.

Once a model is trained, we use it to generate images of a novel, previously unobserved scene in the following way. We use a traditional renderer to render the scene from three random 64×64 camera views (observations). The observations, i.e. the camera parameters, G-buffers, and color images, are passed to the scene encoder to obtain a view-independent scene representation $\mathbf{r}$. To generate a novel view, we pass $\mathbf{r}$ and the parameters of the view (and the G-buffer) to the image generator, which synthesizes a new color image. We use scene representations with 128 to 512 dimensions.

4 COMPOSITIONAL SCENE REPRESENTATION

Our goal in this article is to impose a structure over the neural scene representation such that it respects the orthogonalities between individual scene properties. In Section 4.1, we apply the static partitioning approach of Kulkarni et al. [2015], and extend it to enable adaptive, compressive partitioning of the neural scene representation in Section 4.2. Our method *adaptively disentangles* the lighting, geometry, and material properties of scenes in one dataset, and stores them in disjoint partitions $\mathcal{R}_M$, $\mathcal{R}_L$, and $\mathcal{R}_G$, respectively.

The adaptive partitioning has a number of advantages: (i) it respects the degree of variation of each component, (ii) it improves interpretability of the scene representation and provides insights into the inner mechanisms of different neural architectures—Figure 14, and (iii) it permits basic compositing operations, such as swapping lighting information between different scenes—Section 6.2.

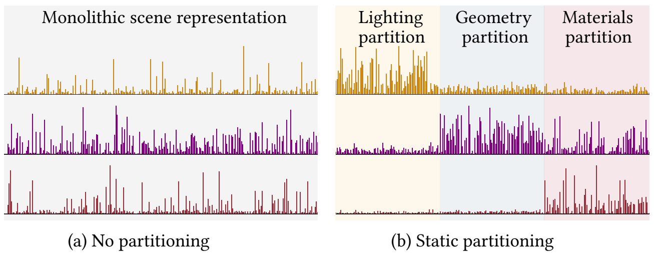

Fig. 5. In contrast to the monolithic scene representation (left) our partitioned scene representation (right) splits scene information into lighting (yellow), geometry (blue), and material (red) partitions. Each row shows the average *standard deviation* in each dimension of the representation when only lighting (top row), geometry and materials (middle row), or only materials (bottom row) are randomized across a large set of scenes.

4.1 Static partitioning

Denoting $\mathcal{R}$ as the latent space of the scene representations, we split $\mathcal{R}$ into three non-overlapping partitions of equal size, $\|\mathcal{R}_M\| \approx \|\mathcal{R}_L\| \approx \|\mathcal{R}_G\| \approx \|\mathcal{R}\|/3$, that will contain (most of) material, lighting, and geometry information. In order to force each partition to hold only the desired information, we adopt the method of Kulkarni et al. [2015] to disentangle scene components by carefully averaging scene representations and adjusting gradients during training.

Specifically, Kulkarni et al. [2015] propose to train networks using batches where only *one* scene property varies. During forward propagation, activations in dimensions that store all the other properties are averaged; these batch-invariant properties should lead to identical activations for all entries in the batch. During backpropagation, the partial derivatives in dimensions for batch-invariant properties are adjusted; the gradient is replaced by its difference from the per-dimension mean. Using the differences nudges the encoder towards producing activations that are closer to the mean.

Example. We may decide to randomize, for instance, the materials across the batch and keep lighting and geometry identical across all batch entries. For each entry we first compute the scene representation with the scene encoder. We then modify activations in lighting and geometry partitions by averaging each dimension across the batch. During backpropagation, we compute loss gradients with respect to the scene representations; one for each entry in the batch. Then we compute the mean partial derivative for each lighting and geometry dimension across the batch, and set the derivative in those dimensions to its difference from the mean. The backpropagation then continues to update the weights of the scene encoder.

The aforementioned algorithm by Kulkarni et al. will ensure that each scene component, i.e. lighting, geometry, and materials, is stored primarily in its own partition. Figure 5 demonstrates the difference between a monolithic and partitioned neural representation. Each bar in the six charts represents the average standard deviation of activations in one dimension across many scenes, where only lighting (top), geometry and materials (middle), or only materials (bottom) are varied. We choose to vary geometry and materials jointly in the middle row since it is difficult to modify geometry without affecting materials. This is a side-effect of changing object visibility in the observation views across a batch.

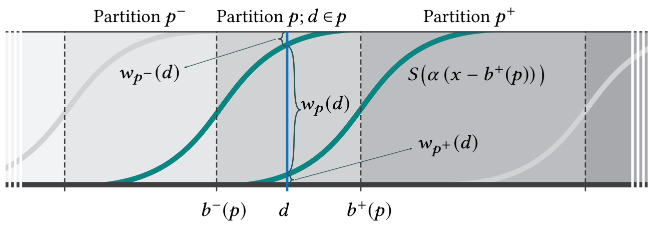

Fig. 6. We adaptively partition the scene representation and assign each dimension d to three consecutive partitions. The contribution of d to a partition is modeled using sigmoids ("S"-shaped curves), which are centered at partition boundaries, and progressively sharpened during optimization.

4.2 Adaptive partitioning

The main drawback of a statically partitioned representation is that it strictly defines the number of bits used to store each scene component, e.g. the lighting partition occupies the first third of the representation. This constraint, which is not present in monolithic representations, is undesired. We now discuss a mechanism for optimizing the partition sizes during training.

For a scene representation with k partitions, we add a trainable tuple $\mathbf{s} := (s_1, \ldots, s_k); s_i \in \mathbb{R}$, to the scene encoder, which defines the sizes of partitions. For the i-th partition, the left boundary $b^-(i)$ and the right boundary $b^+(i)$ are computed by summing up (softmaxed) size parameters of preceding partitions: $b^-(i) = \|\mathcal{R}\| \cdot \sum_{j=1}^{i-1} \sigma(\mathbf{s})_j$, and adding the size of the i-th partition: $b^+(i) = b^-(i) + \|\mathcal{R}\| \cdot \sigma(\mathbf{s})_i$, respectively. The softmax function σ ensures that the learned sizes form a partition of unity.

To allow gradient-based optimization of $\mathbf{s}$, we use fuzzy partition boundaries. A given dimension d of the representation located within a boundary region is shared by multiple partitions: a center partition p, and left and right neighboring partitions, p^- and p^+, respectively. The contribution of dimension d to each partition is given by the following weights:

$$w_p(d) = 1 - w_{p^-}(d) - w_{p^+}(d)\,, \tag{1}$$

$$w_{p^-}(d) = 1 - S\big(\alpha(d - b^-(p))\big)\,, \tag{2}$$

$$w_{p^+}(d) = S\big(\alpha(d - b^+(p))\big)\,, \tag{3}$$

where S is the sigmoid function used to model the fuzzy boundaries; see Figure 6. The parameter α controls the spread of the sigmoid; we progressively increase α during training to approach a step transition in the limit, resulting in a disjoint partitioning.

We treat the representation vector as a circular domain, where the last and first partitions are adjacent. The first partition then acts as the right neighbor of the last partition, and vice versa. All partitions have the same initial size set to $\|\mathcal{R}\|/(k+1)$.

Analysis and discussion. As the optimization progresses, the partitions trade dimensions to best distribute the bits for storing relevant scene properties, as shown in Figures 7 and 8. Initially, the lighting partition grows at the cost of other partitions. This is likely due to the loss function being more sensitive to pixel brightness than to color hue. Once the lighting is predicted sufficiently well, the models focus on extracting material information to correctly predict colors. When converged, the material partition is typically larger than the

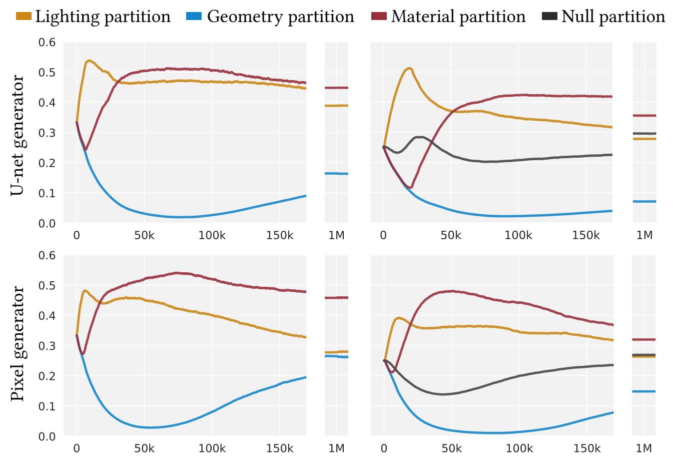

(a) Adaptive partitioning (b) Adaptive w/ null partition (black)

Fig. 7. Adaptive partitioning distributes dimensions of the scene representation between lighting (yellow), geometry (blue), and material (red) components of the scene. The curves show relative sizes of individual partitions and how they evolve during training on the PrimitiveRoom dataset; they stabilize around 1M batches. Note how the partitions become smaller when a null partition (right, black curve) is added to compress the representation.

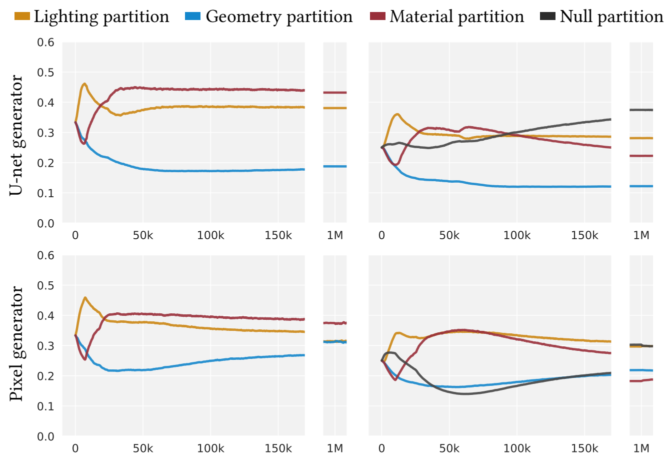

(a) Adaptive partitioning (b) Adaptive w/ null partition (black)

Fig. 8. Same as in Figure 7 but trained on the ArchViz dataset.

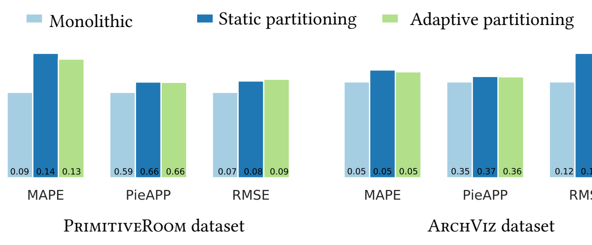

Fig. 9. Average metrics of the pixel generator model with no partitioning, static partitioning, and our adaptive partitioning (lower means better).

lighting partition as lighting in our scenes can be represented with fewer dimensions.

The geometry partition initially shrinks as the generators can rely on the G-buffer (e.g. position and normal buffers). It grows back once lighting effects due to objects that are not directly visible by the camera (e.g. reflections) start dominating the loss. Comparing the U-net generator (top row) and the pixel generator (bottom row) we see that the pixel generator forces the encoder to put more information into the geometry partition. This is to be expected as the pixel generator cannot rely on pixel neighborhoods in the same way as convolutional approaches. In general, the convolutional generators (U-net and GQN analyzed in the supplementary material) utilized the geometry partition less in all our experiments.

In Table 1, we show how the scene representation adapts to datasets with different complexity of lighting and materials. The "many lights" dataset features scenes with up to 10 randomly placed light sources in each scene. The optimization yields a larger lighting partition than in the "many materials" dataset, where scenes contain always a single light source, but the material complexity is doubled compared to the "many lights" dataset.

Table 1. Relative partition sizes of models trained on variations of the PrimitiveRoom dataset with different degrees of material and lighting variation.

	Many lights	Many materials
Lighting partition	39%	30%
Geometry partition	20%	23%
Material partition	37%	43%
Null partition	4%	4%

Performance assessment. In order to analyze the penalties due to imposing static and adaptive partitioning mechanisms, we compare the quality of synthesized images using three error metrics: mean absolute percentage error (MAPE), PieAPP[1] [Prashnani et al. 2018] and root mean square error (RMSE). Figure 9 shows the average performance for (i) a monolithic scene representation, (ii) statically partitioned representation, and (iii) our adaptively partitioned representation. The height of each bar corresponds to the mean value of the metric across 4000 test scenes that were generated using the same recipes as training scenes, but were excluded from training.

Partitioning the representation comes at a penalty in prediction accuracy; similar tradeoffs have been reported in prior work [Nie et al. 2020]. Static partitioning (dark blue) tends to yield the worst results as the static sizes of some partitions may be inappropriately small given the entropy of corresponding scene components. Our adaptive partitioning (green) mitigates this issue by optimizing the bit allocation in the representation, however, it still inherits the tradeoff in prediction accuracy due to enforcing disentanglement.

[1]We first gamma-correct the high dynamic-range images ($\gamma = 2.2$), clip the values to range $[0, 1]$, and quantize them using 8 bits per channel.

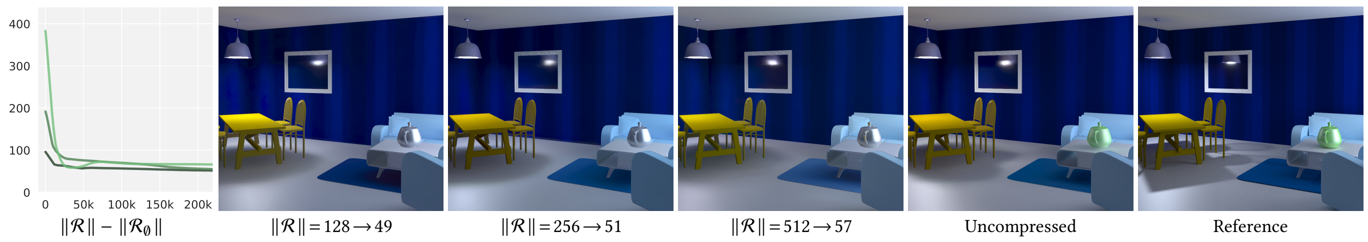
400
300
200
100
0
0
50k
100k
150k
200k
$\|\mathcal{R}\| - \|\mathcal{R}_\emptyset\|$
$\|\mathcal{R}\| = 128 \rightarrow 49$
$\|\mathcal{R}\| = 256 \rightarrow 51$
$\|\mathcal{R}\| = 512 \rightarrow 57$
Uncompressed
Reference

Fig. 10. The null partition allows compressing the scene representation. We plot the total size of *non-null* partitions, $\|\mathcal{R}\| - \|\mathcal{R}_\emptyset\|$, during training for three models with $\|\mathcal{R}\|$ available dimensions equal to 128, 256, and 512. The parameter that controls the compression is identical in all cases; $\beta = 4 \cdot 10^{-4}$. Images labeled with $\|\mathcal{R}\| = X \rightarrow Y$ were rendered after 400k training iterations, at which point the representations shrunk to 49, 51, and 57 dimensions, respectively. Their visual quality is comparable, but lower than in the case of an uncompressed representation; e.g. we lose the color of the teapot.

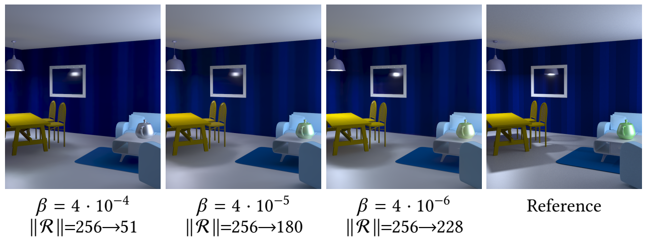
$\beta = 4 \cdot 10^{-4}$
$\|\mathcal{R}\|$=256→51
$\beta = 4 \cdot 10^{-5}$
$\|\mathcal{R}\|$=256→180
$\beta = 4 \cdot 10^{-6}$
$\|\mathcal{R}\|$=256→228
Reference

Fig. 11. Quality of generated images as a function of β, which scales the loss term induced by the total size of material, lighting, and geometry partitions. The differences are best visible on the teapot and on shadows.

4.3 Null partition

Adaptive partitioning allows trading bits of the representation between partitions. However, the scene representation will always use all the available space, even in cases when it could be well-represented using fewer bits. We address this by adding a *null partition* $\mathcal{R}_\emptyset$, which does not influence the image generator, and serves only as a reservoir of unused (available) dimensions.

In order to incentivize the optimization to grow the null partition, and thereby compress the scene representation, we add a penalty term $\beta(\|\mathcal{R}\| - \|\mathcal{R}_\emptyset\|)$ to the loss function, which is proportional to the number of dimensions in all other (non-null) partitions.

Analysis and Discussion. Figures 7 and 8 show the impact of the null partition on the optimization. The partition sizes at 1M iterations better represent the volume of extracted lighting, geometry, and material information than the uncompressed plots (left) as the model utilizes fewer dimensions to represent them.

The null partition removes the burden of guessing the optimal size of the neural scene representation. One can over-allocate the space conservatively and rely on the optimization to grow the null partition appropriately. We confirm this in Figure 10 that plots the total number of lighting, geometry, and material dimensions in three models that initially allocate 128, 256, and 512 dimensions for the representation. All models gradually reduce the number of utilized dimensions to similar counts (49, 51, and 57 dimensions after 400k training iterations); the remaining dimensions are assigned to the null partition. The rendering quality is comparable between the three models, but lower than in the case of uncompressed representation. The tradeoff between the compression ratio and the loss of information can be controlled by adjusting β, as shown in Figure 11.

5 ATTRIBUTION, ANALYSIS, AND IMPROVEMENTS

The partitioning of the scene representation allows us to attribute visual artifacts and poor image quality to specific information that is missing or incomplete in the representation. In this section, we utilize the *gradient* × *input* attribution method [Shrikumar et al. 2017] to measure the sensitivity of generated images to the neural scene representation, the observations, and the G-buffer.

In cases where we compute the attribution of a collection of output values (e.g. for an image patch or an entire partition of the representation) we compute the gradient × input products for individual elements and sum their absolute values to obtain a single attribution scalar.

5.1 Attribution of Partition Activations

In Figure 12, we attribute activations in partitions of the representation to the color, position, and normal channels of two encoded observations. The yellow, blue, and red color shades in the bottom row correspond to attributions of the lighting, geometry, and material partition, respectively. For each pixel, we first compute three attribution scalars—one per partition. Each scalar is then mapped to color shades of the corresponding partition, and the colors are added together. Brighter values indicate higher magnitude of attribution, white signifies high influence on all partitions.

Each partition is attributed to fairly large spatial regions, although certain regions are attributed more than others. For example, high intensities can be observed on the floor, while walls are typically darker. We interpret this as a strong signal that the model specializes to the biases of the dataset, in which most variations occur on the floor (e.g. due to random placement of the furniture and its shadows) and little information needs to be sourced from the walls (only textures and the position of the mirror frame).

The lighting partition (yellow shades) is mainly attributed to regions with visible emitters and to the floor. The emitter intensity needs to be inferred from the color channel, and its contribution can be inferred with the help of additional information in the position and normal channels. We hypothesize that shadow patterns on the floor (color channel), in conjunction with geometry information about the shadow casters (position and normal channels) contribute to the localization and intensity of emitters. In fact, these are the most prominent cues if the emitter is not directly visible in any of the observations. The relatively weak attribution to the wall emitter, specifically to the position and normal channels of observation 2

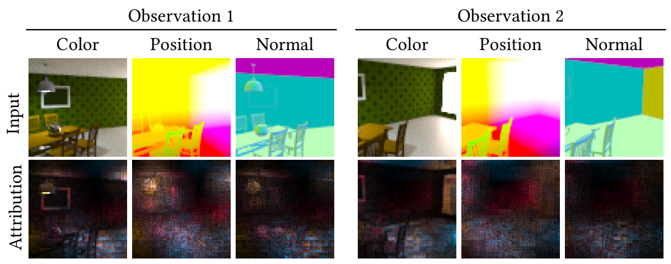

Fig. 12. Attribution of activations in the neural scene representation to the color, position, and normal channels of two observations (top row). The yellow, blue, and red shades in the bottom row correspond to attributions of the lighting, geometry, and material partitions; brighter means stronger attribution.

(right part of the image), is due to its identical placement in all scenes; only its intensity is randomized in the dataset.

The geometry partition (blue shades) is attributed to regions where objects "move" during training. Since the walls are static across the dataset, they have low attributions except for locations where the light fixture or the mirror may appear, as well as locations where the wall may be occluded by another object.

The material partition (red shades) is mainly attributed to regions with randomized materials, such as walls, furniture, and the teapot. It is also attributed to the emitters (albeit not strongly) as the model needs to "undo" the effects of lighting to recover material appearance correctly, and to avoid baking illumination effects into the neural analog of material textures.

Figure 12 attributes entire partitions of the representation. The partitions are responsible for encoding the entire scene such that arbitrary viewpoints can be generated, hence the attributions cover nearly all pixels of the observations and may be hard to interpret precisely. In the next section, we perform a finer analysis by attributing the colors of small pixel regions in the generated image.

5.2 Attribution of Generated Colors

In Figure 13, we attribute generated colors to dimensions in the neural scene representation (middle) and to the observations (left columns) that the representation was extracted from. We use the pixel generator to obtain the generated image.

Reflections. The orange patch focuses on a reflection of a light fixture seen through a mirror surface. Since the corresponding pixels of the G-buffer contain information only about the mirror, and no information about the reflected objects, the generator needs to rely on the scene representation to produce colors of the reflected light fixture. Note that the reflection is in neither of the observations, but the lighting fixture itself is directly observed and the corresponding pixels in the observations have large impact on the reflection; their attribution is high. This indicates that the network is capable of synthesizing view-dependent reflections.

The red patch is placed on a mirror teapot, which reflects large portions of the scene, including the light fixture. The colors in the red patch are thus attributed to all partitions of the representation as reflections require all scene components. In the observations the colors are strongly attributed to the light source as it illuminates the reflected surfaces, but also to the teapot itself when visible.

Materials. The blue patch focuses on the textured wall. The generated colors should depend on the incident illumination and the material of the wall. This is confirmed by the representation attribution, where the lighting partition (yellow background) and material partition (red background) have high attribution values, and also by the observations, where the attribution is high on the light fixture and the walls. Since all textures used during training were periodic, the texture pattern can be detected from any region of the wall, although some regions are preferred over others; we attribute this to biases in the stochastic placement of the camera.

Shadows. The green patch focuses on a shadow boundary due to the table and the light fixture. The representation attributions show that the lighting and geometry partitions are mainly responsible for the synthesis of this shadow region. The material partition is not attributed because we used the same glossy gray material for all floors in the ArchViz dataset. The floor material is thus likely embedded in the generator and the encoder was not forced to extract it. As expected, the shadow boundary is attributed to the light fixture and the pixel region around the table and the chairs in the observations.

5.3 Attribution to Representation and G-buffer

We now study whether the generator relies more on the scene representation or the G-buffer, and demonstrate that this balance may be specific to the architecture of the generator.

In the top row of Figure 14, we analyze the quality of synthesized shadows in a simple scene that contains a cylindrical shadow caster. In the left configuration, the cylinder appears in the camera frustum and is therefore captured by the G-buffer. The generators can rely on the G-buffer to identify its shape and position. In the right configuration, the cylinder is outside of the frustum—we observe only its shadow. The position and shape of the shadow caster can be inferred only *from the neural scene representation.*

The table below the images attributes the predicted colors in the red patches to (i) the partitions of the neural scene representation (top three rows) and (ii) the channels of the G-buffer—we used positions and normals in this experiment (bottom two rows). Each cell in the table was computed by summing the gradient × input values across all elements of the respective partition (or the G-buffer channel) and averaging the sums across the pixels in the red patch. We normalized all values within each column and list them as percentages to drive the focus on relative comparisons.

The table indicates that the pixel generator relies primarily on the neural scene representation (for pixels in the red patch) with the geometry partition being attributed the most (48%). In contrast, the U-net generator barely utilizes the geometry partition (4%) and sources information about geometry almost exclusively from the G-buffer (45% of all attribution). This poses a problem when the shadow caster is outside the camera frustum: the G-buffer contains no information about the caster and the U-net generator is unable to predict the shadow.

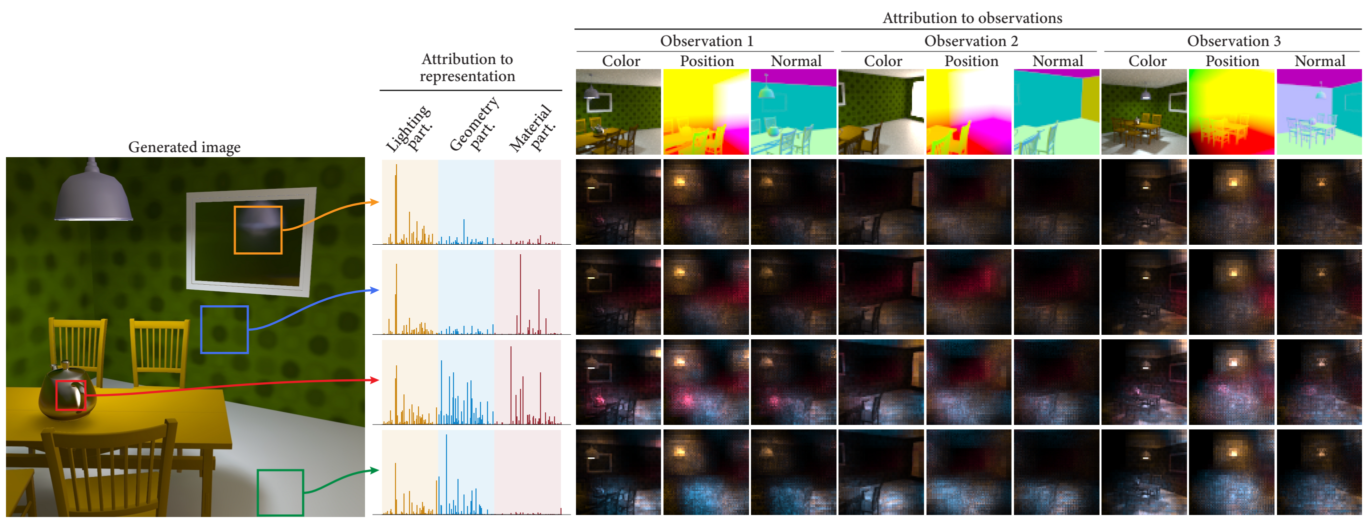

Fig. 13. We attribute the colors of four patches in a generated image (left) to dimensions in the neural scene representation (middle), and to the color, position, and normal channels of the three observations (right) that the representation was extracted from. Each bar in the attribution histograms shows the contribution of one dimension of the representation to the patch; the bar height corresponds to the aggregate attribution. On the right, we propagate the attribution through each partition to individual observations and their channels. A blue shade, for instance, indicates that an observation pixel contributed geometry information (through the geometry partition) to the generated patch; the brightness corresponds to the aggregate attribution.

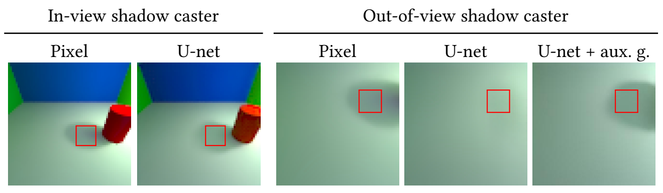

	In-view Pixel	In-view U-net	Out-of-view Pixel	Out-of-view U-net	Out-of-view U-net + aux. g.
Attributions to neural representation					
light:	22%	43%	22%	34%	29%
geo.:	48%	4%	49%	10%	17%
mat.:	13%	8%	15%	13%	12%
	82%	**55%**	**86%**	**56%**	**58%**
Attributions to G-buffer					
pos.:	9%	26%	5%	24%	21%
norm.:	8%	19%	10%	20%	21%
	18%	**45%**	**14%**	**44%**	**42%**

Fig. 14. Shadow synthesis in a scene with a directly visible shadow caster (left pair) and with the same shadow caster being out of the view (right tripple). The pixel generator and the U-net generator are both able to synthesize shadows of *visible* shadow casters. However, when the caster is out of the view, the U-net fails to produce the shadow since it relies primarily on the G-buffer. This is evidenced in the table below that lists relative attributions (gradient × input) averaged over the marked pixels. Combining the U-net generator with an auxiliary *pixel* generator increases the attribution to the geometry partition, from 10% to 17%, and helps the U-net to correctly synthesize the shadow.

The results of this comparison are not entirely unexpected. Pixel generators, which access one pixel at a time, force the encoder to put more information about the geometry into the scene representation (as already suggested by Figures 7 and 8) and their performance is thus less impacted by the content of the G-buffer. The U-net generator—being convolutional—has a strong ability to source information from pixel neighborhoods in the G-buffer, but fails when the G-buffer lacks key information. This occurs whenever objects occlude each other or reflect surfaces not present in the view. The resulting artifacts are distracting, but do not appear sufficiently often during training to "teach" the U-net generator to utilize the geometry partition of the neural representation. We address this issue in the next section.

5.4 Auxiliary Generators

Our goal here is to force the scene encoder to extract information that may be underrepresented, but vital for good performance in certain situations. We employ an auxiliary generator [Philip et al. 2019] that is trained concurrently with the main generator, but focuses on the failure cases.

Specifically, to rectify the poor performance of the U-net generator on shadows due to invisible casters, we add a pixel generator that is optimized to produce shadows—grayscale images of (partial) visibility of light sources. The output of the auxiliary "shadow" generator is fed into the U-net generator. The loss function of the auxiliary generator is the same as the loss function of the main generator; except we evaluate it on reference shadow images. The losses are summed together.

Adding the auxiliary generator can be interpreted as changing the loss function, but it has the key benefit of impacting *primarily* the scene encoder of the original model; it keeps the loss of the original generator intact. Since both generators use the same scene representation during training, the auxiliary generator steers the encoder to extract the missing information. The second, and likely the key benefit in this specific case, is the shadow image that the auxiliary generator provides to the U-net. The right column in Figure 14 illustrates the improvement of the U-net generator after adding the auxiliary shadow (pixel) generator—the model draws more information from the geometry partition (the attribution increases from 10% to 17%) and succeeds in synthesizing the shadow.

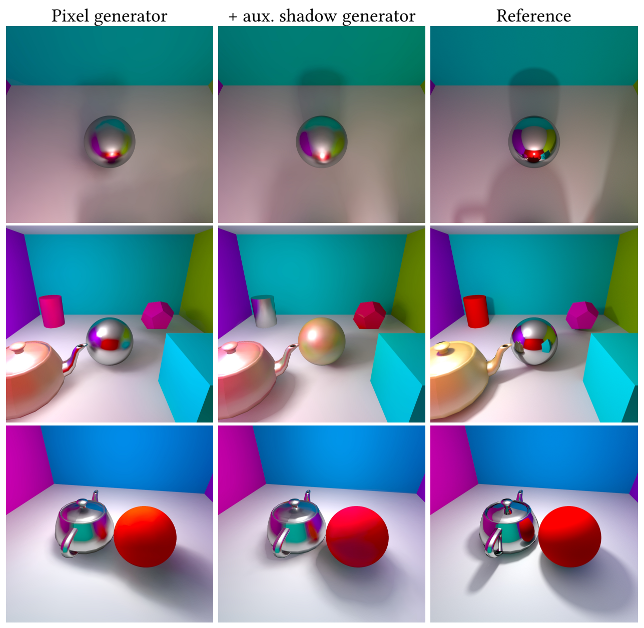

Fig. 15. Adding an auxiliary shadow (pixel) generator steers the encoder to focus more on geometric and lighting information, which improves the synthesis of shadows, albeit at the cost of encoding materials.

We also tested whether the auxiliary shadow generator can improve the performance of *pixel* generators. The increase in visual quality is subtle but still noticeable; Figure 15 shows three examples. The impact on the partitioning is more pronounced; Figure 16 and Table 2 confirm the growth of the geometry partition at the cost of the material partition. As a result, materials tend to be captured with lower accuracy. This can be observed on some of the objects (see the middle row of Figure 15). Adding an auxiliary generator thus does not necessarily lead to better overall results—quantitative metrics remained unaffected in this case—but rebalances the focus of the encoder.

6 APPLICATIONS

In this section, we explore two possible applications that (compositional) neural scene representations could improve in the future.

6.1 Rendering Indirect Illumination

One shortcoming of the neural model employed in this article (up to this point) is the rather poor visual quality on high-frequency visual features. However, the fine details and structures due to local illumination can be synthesized inexpensively using classical methods (if an accurate 3D model is available). The output from the classical renderer can be provided to the neural renderer as an additional input, or simply combined with the generated image. The two renderers can complement each other with the neural one focusing on the costly effects only.

We investigate one such scenario in Figure 17: we compute direct illumination via ray tracing and optimize the neural model to produce only indirect illumination. We augment the G-buffer to

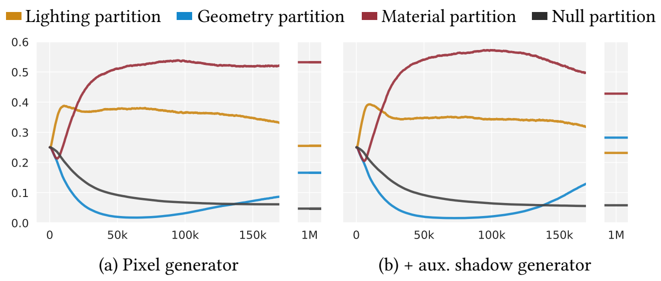

Fig. 16. A model with a single pixel generator (left) can be steered towards extracting more geometry information (blue) by adding an auxiliary shadow generator (right).

Table 2. Relative partition sizes for the models from Figure 15 and Figure 16 after one million of training iterations.

	Pixel generator	+ aux. shadow generator
Lighting partition	25%	23%
Geometry partition	17%	28%
Material partition	53%	43%
Null partition	5%	6%

include material information (diffuse albedo and surface roughness); this improves material encoding and synthesis quality. Lastly, the ray-traced image is also input into the neural generator, allowing it to learn direct-to-indirect radiance transfer; this works remarkably well with convolutional architectures [Nalbach et al. 2017].

In our experiments, however, we used the pixel generator that upscales the scene information (learned at low resolutions) to high resolutions more gracefully than the U-net generator (see the comparisons of different generators in the supplementary material). The test scenes feature notable interreflection between objects, e.g. between teapots and tables or between sofas and pillows, that are synthesized fairly well. Indirect illumination over long distances, such as the yellow tint on the ceiling (top row) due to light bouncing off the carpet and sofas, is reproduced by the neural model as well.

Our unoptimized implementation utilizing PyTorch for inference and accelerating tracing of rays using Optix required: 7 minutes to trace the direct-illumination buffer (8k spp), and 400 ms to predict the indirect-illumination; both at 1k×1k resolution using an NVIDIA RTX 6000 GPU. Path-tracing the indirect-illumination references (8k spp) required 25 minutes; we list this merely for completeness and leave comparisons to state-of-the-art GI renderers for future work.

6.2 Editing in Latent Space

We can exploit the compositionality of our neural scene representation to perform scene edits directly on the (latent) scene representation. The task of transferring information between latent codes of different scenes is challenging for monolithic representations that do not feature a clear separation of individual components. As long as the scene representation is appropriately partitioned, such edits become straightforward.

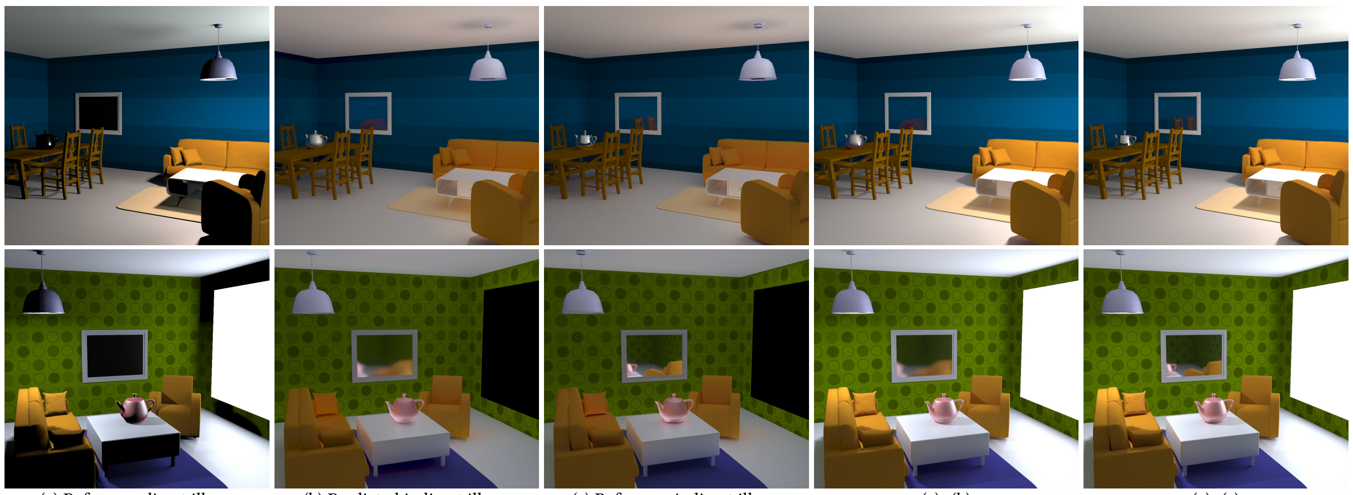
(a) Reference direct illum.
(b) Predicted indirect illum.
(c) Reference indirect illum.
(a)+(b)
(a)+(c)

Fig. 17. Neural synthesis of indirect illumination. The neural model is optimized to predict indirect illumination only from the neural scene representation, G-buffer w/ geometry and material information, and the direct illumination buffer. Results show that both local and distant interreflections are synthesized fairly accurately. Predictions of mirror reflections (teapot in top row and mirror in bottom row) suffer from overbluring. The supplementary material describes a possible remedy by including information about reflection rays in the G-buffer.

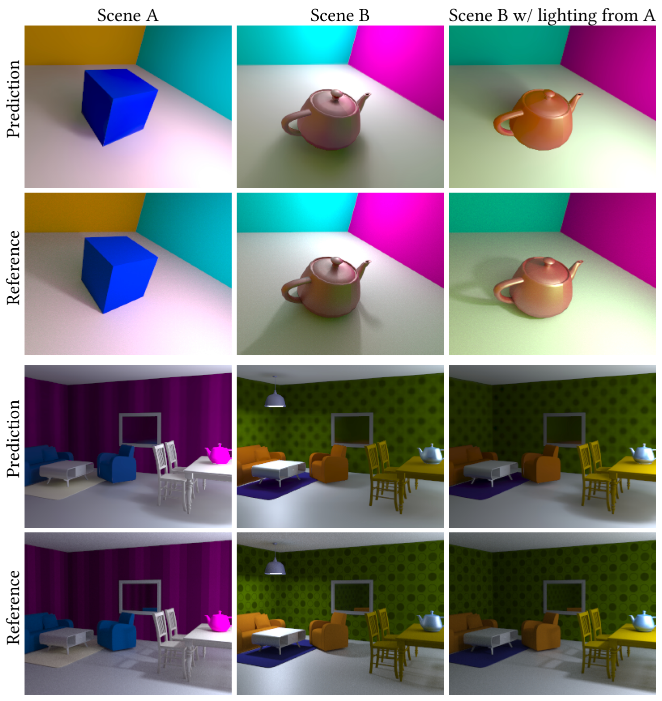

Fig. 18. Examples of relighting application, where the lighting partition of scene A replaces the lighting partition of scene B. The relighting result is shown in the right column.

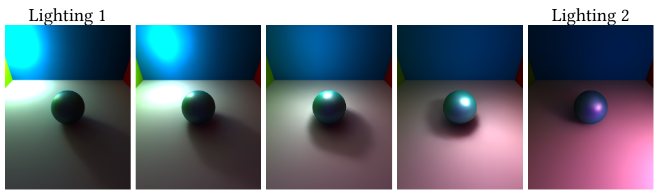

Fig. 19. Lighting partition interpolation, where the interpolation endpoints were extracted from lighting partitions of two other scenes, shows that indirect color bleeding and specular highlights are correctly synthesized even though the material partition remains constant. This proves that the model has learned to properly separate materials from lighting.

In Figure 18, we replace the lighting partition in the representation of Scene B with the lighting partition of Scene A. We then feed the composited representation and the G-buffer of Scene B into the pixel generator. The generated image is shown in the third column; reference renderings are included below. The shadows and highlights are repositioned correctly in both studied cases.

One could also exercise the idea of transfering materials. Our model supports this as long as the two scenes have identical geometry, i.e. the mapping of materials to objects is identical in both scenes and transferring the material partition merely changes the material definition. When the scenes differ in geometry, material transfer requires deeper understanding of the content (e.g. semantic roles of individual surfaces) to map material sources to targets.

In Figure 19, we perform a linear interpolation between two lighting configurations to demonstrate that highlights and shadows move gradually, as if the light source was moving, instead of blending intensities of two light sources; see the supplementary video for additional animations.

7 DISCUSSION AND FUTURE WORK

Implicit vs. explicit disentanglement. Neural representations tend to be naturally disentangled to some degree, as demonstrated with GQNs using scene algebra experiments [Eslami et al. 2018] or with VAEs by manipulating latent variables [Higgins et al. 2017]. These

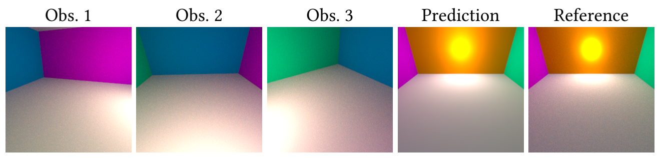

Fig. 20. The model is capable of extracting the color of the orange wall from indirect lighting in the observations when the wall is not observed directly.

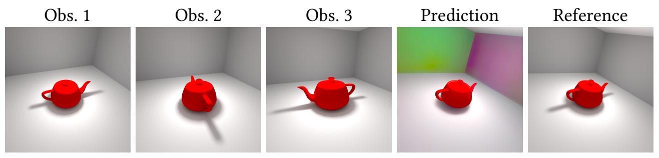

Fig. 21. An example of poor generalization of the model to a scene with "unknown" materials; gray color was never used for the walls in the training dataset, only for the floor and the ceiling. The model incorrectly maps the gray color of the walls in the observations to shades of green and pink.

approaches put fewer constraints on the model than our method, but they may not yield the desired, or full disentanglement.

Explicit partitioning provides means to enforce constraints that the model should never violate. Our adaptive partitioning scheme can mitigate performance penalty of static partitioning due to improperly allocating bits in the scene representation. However, the negative impact of disentanglement on the quality of the image synthesis remains. Designing disentanglement and partitioning techniques that retain the performance of monolithic representations is an important direction for future research.

In this article, the content of individual partitions is orthogonal. Having a clear separation between the scene components has two distinct benefits. First, the explicit partitioning facilitates a straightforward attribution analysis that offers valuable insights into the inner workings of different neural models (see Figure 14). Second, it enables basic scene compositing operations, such as relighting through the swapping of lighting partitions (Figure 18). It is worth noting that explicit partitioning does not preclude discovering additional factors of variation using different methods. Striking a good balance between the two is an interesting topic for future research.

Fine-grained compositionality. We partition the scene information at a very coarse level: materials, lighting, and geometry. We view this as the first step towards truly compositional, modular representations that will enable building complex scenes from smaller modules. Such (hierarchical) scene representations will allow fine-grained edits, for instance replacing the material of one specific object with the material of another object, possibly from a different scene. Enforcing compositionality at a finer level is an important goal that we hope future work will achieve.

Generalization and challenging cases. Our model is capable of extracting subtle clues from indirect illumination, e.g. to correctly predict the material of an unobserved wall (see Figure 20). However, it sometimes struggles with seemingly simple configurations (see Figure 21), if they were not encountered during training. While concerning, this limitation is not specific to our approach and other works in the domain suffer from poor generalization as well. We expect refined compositionality of the scene representation to play a central role also in addressing generalization issues.

Validity of design decisions. We deliberately restricted the use of classical rendering algorithms to a specific subset of image buffers. This was done with the intent of facilitating the analysis of the inner workings of the model, for instance by providing *no* material and lighting information in the G-buffer when studying attribution in Figure 12.

In Figure 17, we departed from the clear separation and added material information to the G-buffer. The final image was obtained by combining outputs from a classical and a neural renderer; we expect such splits of the rendering task to be most rewarding in the future. We also note that specular and glossy reflections can be further improved by including parameters of perfect-reflection rays; see the supplementary material for additional results.

Another decision worth revisiting is the extraction of the scene representation from a set of image buffers. The observations have the benefit of including all effects of global light transport that we strive to synthesize, but other forms of input, e.g. omnimaps, voxel representations, unstructured sets of radiance estimates, light fields, or textual descriptions could suit specific applications better.

8 CONCLUSION

We extended the disentanglement technique of Kulkarni et al. [2015] to respect the entropy of individual components and applied it to neural scene representations to adaptively partition lighting, geometry, and material information. By adding the null partition, which serves as a reservoir of available bits during training, we extract compressed neural representations of the scene.

Our experiments highlight the desirable properties offered by adaptive partitioning, namely the enhanced interpretability and control. Specifically, we were able to refine existing attribution methods to reveal whether pixels in observations influenced the final synthesized pixel values through the lighting, geometry, and/or material information encoded in the scene representation. We also studied the artifacts of different image generators, and propose to fix poor performance by adding an auxiliary generator that steers the scene encoding towards information that is otherwise missing from the neural scene representation.

Yet, the results generated by most models in this paper suffer from visual artifacts. We thus investigated a scenario, where the neural renderer generates indirect illumination only to complement a classical ray tracer; we believe complementing traditional graphics algorithms, rather than replacing them, is a fruitful direction for future research if production rendering is the ultimate goal.

Addressing the quality and scaling remains a priority for future work as artifacts may not go away by merely increasing the size of networks and datasets. We believe that imposing additional constraints and principles of light transport over neural models will be necessary to yield realistically looking images. Understanding the inner workings of a model will be paramount for injecting these constraints; our work presents an important step in that direction.

ACKNOWLEDGMENTS

We thank Jacob Munkberg, Jon Hasselgren, Marco Salvi, Pontus Andersson, Till Schnabel, and the anonymous reviewers for constructive feedback. We also thank Jaakko Lehtinen, S. M. Ali Eslami, Cengiz Öztireli, and Marco Ancona for fruitful discussions, and Jay-Artist, Wig42, dpamplin, Wolgraph, MZiemys, SlykDrako, Tsukiyono, and CtrlArt MDL for models and textures.

REFERENCES

Marco Ancona, Enea Ceolini, Cengiz Öztireli, and Markus Gross. 2018. Towards better understanding of gradient-based attribution methods for Deep Neural Networks. In *International Conference on Learning Representations*.

Yoshua Bengio, Aaron Courville, and Pascal Vincent. 2013. Representation Learning: A Review and New Perspectives. *IEEE Transactions on Pattern Analysis and Machine Intelligence* 35, 8 (2013), 1798–1828.

Xi Chen, Yan Duan, Rein Houthooft, John Schulman, Ilya Sutskever, and Pieter Abbeel. 2016. InfoGAN: Interpretable Representation Learning by Information Maximizing Generative Adversarial Nets. In *Advances in Neural Information Processing Systems 29*. Curran Associates, Inc., 2172–2180.

Paul Debevec. 1998. Rendering Synthetic Objects into Real Scenes: Bridging Traditional and Image-Based Graphics with Global Illumination and High Dynamic Range Photography. In *Proceedings of the 25th Annual Conference on Computer Graphics and Interactive Techniques (SIGGRAPH '98)*. Association for Computing Machinery, New York, NY, USA, 189–198. https://doi.org/10.1145/280814.280864

Paul Debevec, Tim Hawkins, Chris Tchou, Haarm-Pieter Duiker, Westley Sarokin, and Mark Sagar. 2000. Acquiring the Reflectance Field of a Human Face. In *Proceedings of the 27th Annual Conference on Computer Graphics and Interactive Techniques (SIGGRAPH '00)*. ACM Press/Addison-Wesley Publishing Co., USA, 145–156. https://doi.org/10.1145/344779.344855

Valentin Deschaintre, Miika Aittala, Frédo Durand, George Drettakis, and Adrien Bousseau. 2019. Flexible SVBRDF Capture with a Multi-Image Deep Network. *Computer Graphics Forum* 38, 4 (2019), 1–13. https://doi.org/10.1111/cgf.13765

Mengnan Du, Ninghao Liu, and Xia Hu. 2019. Techniques for Interpretable Machine Learning. *Commun. ACM* 63, 1 (Dec. 2019), 68–77. https://doi.org/10.1145/3359786

S. M. Ali Eslami, Danilo Jimenez Rezende, Frederic Besse, Fabio Viola, Ari S. Morcos, Marta Garnelo, Avraham Ruderman, Andrei A. Rusu, Ivo Danihelka, Karol Gregor, David P. Reichert, Lars Buesing, Theophane Weber, Oriol Vinyals, Dan Rosenbaum, Neil Rabinowitz, Helen King, Chloe Hillier, Matt Botvinick, Daan Wierstra, Koray Kavukcuoglu, and Demis Hassabis. 2018. Neural scene representation and rendering. *Science* 360, 6394 (2018), 1204–1210. https://doi.org/10.1126/science.aar6170

P. Hermosilla, S. Maisch, T. Ritschel, and T. Ropinski. 2019. Deep-learning the Latent Space of Light Transport. *Computer Graphics Forum* 38, 4 (2019), 207–217. https://doi.org/10.1111/cgf.13783

Irina Higgins, Loïc Matthey, Arka Pal, Christopher Burgess, Xavier Glorot, Matthew M Botvinick, Shakir Mohamed, and Alexander Lerchner. 2017. beta-VAE: Learning Basic Visual Concepts with a Constrained Variational Framework. In *Proc. ICLR*.

Simon Kallweit, Thomas Müller, Brian Mcwilliams, Markus Gross, and Jan Novák. 2017. Deep Scattering: Rendering Atmospheric Clouds with Radiance-Predicting Neural Networks. *ACM Trans. Graph.* 36, 6, Article Article 231 (Nov. 2017), 11 pages. https://doi.org/10.1145/3130800.3130880

Tero Karras, Timo Aila, Samuli Laine, and Jaakko Lehtinen. 2018. Progressive Growing of GANs for Improved Quality, Stability, and Variation. In *International Conference on Learning Representations*.

Hyeongwoo Kim, Pablo Garrido, Ayush Tewari, Weipeng Xu, Justus Thies, Matthias Nießner, Patrick Pérez, Christian Richardt, Michael Zollhöfer, and Christian Theobalt. 2018. Deep Video Portraits. *ACM Trans. Graph.* 37, 4, Article Article 163 (July 2018), 14 pages. https://doi.org/10.1145/3197517.3201283

Diederik P. Kingma and Jimmy Ba. 2015. Adam: A Method for Stochastic Optimization. In *International Conference on Learning Representations*.

Tejas D Kulkarni, William F. Whitney, Pushmeet Kohli, and Josh Tenenbaum. 2015. Deep Convolutional Inverse Graphics Network. In *Advances in Neural Information Processing Systems 28*. Curran Associates, Inc., 2539–2547.

Stephen Lombardi, Tomas Simon, Jason Saragih, Gabriel Schwartz, Andreas Lehrmann, and Yaser Sheikh. 2019. Neural Volumes: Learning Dynamic Renderable Volumes from Images. *ACM Trans. Graph.* 38, 4, Article Article 65 (July 2019), 14 pages. https://doi.org/10.1145/3306346.3323020

Wojciech Matusik. 2003. *A data-driven reflectance model*. Ph.D. Dissertation. Massachusetts Institute of Technology.

Thomas Müller, Brian McWilliams, Fabrice Rousselle, Markus Gross, and Jan Novák. 2019. Neural Importance Sampling. *ACM Trans. Graph.* 38, 5, Article 145 (Oct. 2019), 19 pages. https://doi.org/10.1145/3341156

O. Nalbach, E. Arabadzhiyska, D. Mehta, H.-P. Seidel, and T. Ritschel. 2017. Deep Shading: Convolutional Neural Networks for Screen Space Shading. *Comput. Graph. Forum* 36, 4 (July 2017), 65–78. https://doi.org/10.1111/cgf.13225

Phong Nguyen-Ha, Lam Huynh, Esa Rahtu, and Janne Heikkilä. 2019. Predicting Novel Views Using Generative Adversarial Query Network. In *Image Analysis*. Springer International Publishing, Cham, 16–27.

Thu Nguyen-Phuoc, Chuan Li, Lucas Theis, Christian Richardt, and Yong-Liang Yang. 2019. HoloGAN: Unsupervised Learning of 3D Representations From Natural Images. In *The IEEE International Conference on Computer Vision (ICCV)*.

Thu H Nguyen-Phuoc, Chuan Li, Stephen Balaban, and Yongliang Yang. 2018. RenderNet: A deep convolutional network for differentiable rendering from 3D shapes. In *Advances in Neural Information Processing Systems 31*. Curran Associates, Inc., 7891–7901.

Weili Nie, Tero Karras, Animesh Garg, Shoubhik Debhath, Anjul Patney, Ankit B. Patel, and Anima Anandkumar. 2020. Semi-Supervised StyleGAN for Disentanglement Learning. arXiv:cs.CV/2003.03461

Kyle Olszewski, Sergey Tulyakov, Oliver Woodford, Hao Li, and Linjie Luo. 2019. Transformable Bottleneck Networks. *The IEEE International Conference on Computer Vision (ICCV)* (Nov 2019).

Julien Philip, Michaël Gharbi, Tinghui Zhou, Alexei A. Efros, and George Drettakis. 2019. Multi-View Relighting Using a Geometry-Aware Network. *ACM Trans. Graph.* 38, 4, Article Article 78 (July 2019), 14 pages. https://doi.org/10.1145/3306346.3323013

Ekta Prashnani, Hong Cai, Yasamin Mostofi, and Pradeep Sen. 2018. PieAPP: Perceptual Image-Error Assessment Through Pairwise Preference. In *The IEEE Conference on Computer Vision and Pattern Recognition (CVPR)*.

Konstantinos Rematas and Vittorio Ferrari. 2019. Neural Voxel Renderer: Learning an Accurate and Controllable Rendering Tool. arXiv:cs.CV/1912.04591

Peiran Ren, Jiaping Wang, Minmin Gong, Stephen Lin, Xin Tong, and Baining Guo. 2013. Global Illumination with Radiance Regression Functions. *ACM Trans. Graph.* 32, 4, Article 130 (July 2013), 12 pages. https://doi.org/10.1145/2461912.2462009

Olaf Ronneberger, Philipp Fischer, and Thomas Brox. 2015. U-Net: Convolutional Networks for Biomedical Image Segmentation. In *Medical Image Computing and Computer-Assisted Intervention – MICCAI 2015*. Springer International Publishing, Cham, 234–241.

Dan Rosenbaum, Frederic Besse, Fabio Viola, Danilo J. Rezende, and S. M. Ali Eslami. 2018. Learning models for visual 3D localization with implicit mapping. arXiv:cs.CV/1807.03149

Avanti Shrikumar, Peyton Greenside, and Anshul Kundaje. 2017. Learning Important Features Through Propagating Activation Differences. In *Proceedings of the 34th International Conference on Machine Learning*, Vol. 70. PMLR, Sydney, Australia, 3145–3153.

Vincent Sitzmann, Michael Zollhöfer, and Gordon Wetzstein. 2019. Scene Representation Networks: Continuous 3D-Structure-Aware Neural Scene Representations. In *Advances in Neural Information Processing Systems 32*. Curran Associates, Inc., 1119–1130.

Maxim Tatarchenko, Alexey Dosovitskiy, and Thomas Brox. 2016. Multi-view 3D Models from Single Images with a Convolutional Network. In *Computer Vision – ECCV 2016*. Springer International Publishing, Cham, 322–337.

Ayush Tewari, Ohad Fried, Justus Thies, Vincent Sitzmann, Stephen Lombardi, Kalyan Sunkavalli, Ricardo Martin-Brualla, Tomas Simon, Jason Saragih, Matthias Nießner, Rohit Pandey, Sean Fanello, Gordon Wetzstein, Jun-Yan Zhu, Christian Theobalt, Maneesh Agrawala, Eli Shechtman, Dan B Goldman, and Michael Zollhöfer. 2020. State of the Art on Neural Rendering. arXiv:cs.CV/2004.03805

Justus Thies, Michael Zollhöfer, and Matthias Nießner. 2019. Deferred Neural Rendering: Image Synthesis Using Neural Textures. *ACM Trans. Graph.* 38, 4, Article Article 66 (July 2019), 12 pages. https://doi.org/10.1145/3306346.3323035

Joshua Tobin, Wojciech Zaremba, and Pieter Abbeel. 2019. Geometry-Aware Neural Rendering. In *Advances in Neural Information Processing Systems 32*. Curran Associates, Inc., 11555–11565.

Delio Vicini, Vladlen Koltun, and Wenzel Jakob. 2019. A Learned Shape-Adaptive Subsurface Scattering Model. *ACM Trans. Graph.* 38, 4, Article Article 127 (July 2019), 15 pages. https://doi.org/10.1145/3306346.3322974

Jörg Wagner, Jan Mathias Köhler, Tobias Gindele, Leon Hetzel, Jakob Thaddäus Wiedemer, and Sven Behnke. 2019. Interpretable and Fine-Grained Visual Explanations for Convolutional Neural Networks. In *The IEEE Conference on Computer Vision and Pattern Recognition (CVPR)*.

Matthew D. Zeiler and Rob Fergus. 2014. Visualizing and Understanding Convolutional Networks. In *Computer Vision – ECCV 2014*. Springer International Publishing, Cham, 818–833.

Quan Zheng and Matthias Zwicker. 2019. Learning to Importance Sample in Primary Sample Space. *Computer Graphics Forum* 38, 2 (2019), 169–179. https://doi.org/10.1111/cgf.13628